

01 Jan 2014


Crystallization in Nano-Confinement Seeded by a Nanocrystal – A Molecular Dynamics Study

Heng Pan

Missouri University of Science and Technology, hp5c7@mst.edu

Costas Grigoropoulos

Follow this and additional works at: https://scholarsmine.mst.edu/mec_aereng_facwork

 Part of the [Aerospace Engineering Commons](#), [Mechanical Engineering Commons](#), and the [Numerical Analysis and Scientific Computing Commons](#)

Recommended Citation

H. Pan and C. Grigoropoulos, "Crystallization in Nano-Confinement Seeded by a Nanocrystal – A Molecular Dynamics Study," *Journal of Applied Physics*, vol. 115, no. 10, American Institute of Physics (AIP), Jan 2014.

The definitive version is available at <https://doi.org/10.1063/1.4868465>

This Article - Journal is brought to you for free and open access by Scholars' Mine. It has been accepted for inclusion in Mechanical and Aerospace Engineering Faculty Research & Creative Works by an authorized administrator of Scholars' Mine. This work is protected by U. S. Copyright Law. Unauthorized use including reproduction for redistribution requires the permission of the copyright holder. For more information, please contact scholarsmine@mst.edu.

Crystallization in nano-confinement seeded by a nanocrystal—A molecular dynamics study

Heng Pan^{1,a)} and Costas Grigoropoulos^{2,a)}

¹Department of Mechanical & Aerospace Engineering, Missouri University of Science and Technology, Rolla, Missouri 65409, USA

²Department of Mechanical Engineering, University of California-Berkeley, Berkeley, California 94720, USA

(Received 26 October 2013; accepted 3 March 2014; published online 13 March 2014)

Seeded crystallization and solidification in nanoscale confinement volumes have become an important and complex topic. Due to the complexity and limitations in observing nanoscale crystallization, computer simulation can provide valuable details for supporting and interpreting experimental observations. In this article, seeded crystallization from nano-confined liquid, as represented by the crystallization of a suspended gold nano-droplet seeded by a pre-existing gold nanocrystal seed, was investigated using molecular dynamics simulations in canonical (NVT) ensemble. We found that the crystallization temperature depends on nano-confinement volume, crystal orientation, and seed size as explained by classical two-sphere model and Gibbs-Thomson effect. © 2014 AIP Publishing LLC. [<http://dx.doi.org/10.1063/1.4868465>]

I. INTRODUCTION

The crystallization of amorphous materials is a critical manufacturing process in silicon based electronics, thin film transistors,¹ displays,² and thin-film solar cell devices.³ Thermal annealing step is involved to convert the as-deposited materials to single crystal structures. Conventional furnace, rapid thermal process, or laser annealing can be chosen for specific thermal budget and temperature requirements. Recently, nanoscale crystallization, particularly crystallization in nano-confinement, has drawn substantial interests. Single crystal Ge or Si can be obtained through rapid-melt-growth from Si seeds,^{4–6} lateral epitaxial growth on silicon oxide from underlying seeds,^{7,8} and solid-phase-epitaxy from Si nanowire seeds.⁹ Arora *et al.* describe the manufacturing of single crystal confined in nanostructures by laser induced crystallization of amorphous materials on seeding substrate.¹⁰ Nanoscale crystallization using nanoscale nanosecond laser was reported by Chimmalgi *et al.*¹¹ and TEM observation of the crystallization was reported by Xiang *et al.*¹² Nanocrystallization of amorphous TiO₂ nanofilms by laser annealing has been reported by Overschelde *et al.*¹³ Laser melting and crystallization of metal oxide nanoparticles have been reported to fabrication TFTs¹⁴ and solar cells.¹⁵

It is desirable to gain in-depth understanding on effects of temperatures, nano-confinement dimensions, crystal orientation on crystallization process, and resultant nanostructure quality. Despite vast experimental and simulation studies on crystallization from bulk melt, systematic studies on nano-confined crystallization are still lacking,¹⁶ especially related to transition temperature and atomic defect evolutions. Figure 1 illustrates that the difference in crystallization processes occurs in bulk (a) versus in nano-confined volumes (b)-(d). It is clear the phase transition temperatures

and defect evolutions in (a) will be very different from (b)-(d) due to the absence of confining surfaces in (a). There are subtle differences among (b)-(d): Fig. 1(b)—with the solid seed located inside the droplet, Fig. 1(c)—with the seed located on the boundary, and Fig. 1(d)—depicting that the substrate serves as seed.

In order to understand the crystallization transition temperatures described in Figs. 1(a)–1(d), a review of macroscopic thermodynamic models is helpful. Several interesting melting related phenomena have been well documented, including the size-dependent depression of the melting point,¹⁷ the coexistence of a solid core and a liquid shell during melting,¹⁸ and the superheating in nanoclusters.¹⁹ Chemical equilibrium condition of a solid and a liquid particle of identical size is expressed by the Pawlow equation²⁰

$$T_{m1} - T_0 = -\frac{2T_0v}{R_s\Delta H} \left(\gamma_{sv} - \gamma_{lv} \left(\frac{\rho_s}{\rho_l} \right)^{2/3} \right), \quad (1)$$

where T_0 is the melting point of the bulk system, T_{m1} is the melting point the solid particle, R_s is the radius of the solid particle, ΔH is the latent heat of melting per atom, v is the atomic volume, and γ_{sv} and γ_{lv} are the solid-vapor and liquid-vapor interfacial energies, respectively. The well-known equation by Buffat and Borel¹⁷ has been developed

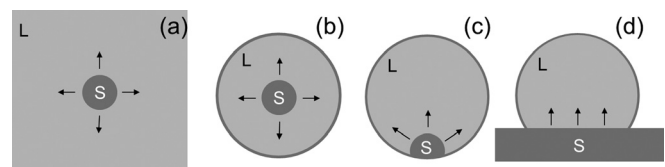


FIG. 1. Schematic diagrams showing typical scenarios of crystallizations in bulk and confined volumes. (a) in bulk system; (b) crystal seed is located at the center of a confined liquid volume; (c) crystal seed is located at the edge of a confined liquid volume; (d) a confined liquid volume crystallizes by seeding substrate.

^{a)}Authors to whom correspondence should be addressed. Electronic addresses: nanofab@gmail.com and cgrigoro@me.berkeley.edu

along the same theoretical foundation. Reiss and Wilson introduced a surface melting layer and considered the coexistence of the solid core and liquid shell in the nanoparticle.^{21,22}

On the other side, in describing the onset of crystallization, the critical nucleus size in homogeneous nucleation in bulk liquid is rewritten as

$$T_{m1} - T_0 = -\frac{2T_0\gamma_{sl}}{r^*\Delta H}, \quad (2)$$

where r^* is the critical nuclei size. The above equations all follow the form $T_{m1} - T_0 = 2\frac{b}{R} + c$ that relates the transition temperatures (melting and crystallization) with the solid particle size R . It is worthy pointing out that the pre-factor 2 originates from the unstable chemical potential equilibrium assumption between the solid and liquid. For the case of nucleation, the equilibrium condition can be found when $dG/dR = 0$, where G is the Gibbs free energy. A stricter requirement is $dG < 0$ as a result of nuclei growth, which dictates a pre-factor of 3 for the crystallization temperature.¹⁶

The above mentioned macroscopic thermodynamic models form the basics to understand crystallizations in Figures 1(a)–1(d). It is known these macroscopic models can be insufficient in describing nanoscale phenomena.^{23–25} For example, Nam *et al.*²³ and Mendez-Villuendas *et al.*²⁴ both point out that nucleation initiates from surfaces of gold droplets, even though bulk thermodynamic model $\gamma_{sv} \geq \gamma_{sl} + \gamma_{lv}$ and reported surface energy data for gold could not allow surface nucleation thermodynamically. Shibuta²⁶ employed molecular dynamics simulation to study phase transition in bcc metal nanoparticles. They found that the melting point can be well modeled by the inverse of particle radius, suggesting compliance with the Gibbs-Thomson effect, while the depression of the nucleation point exhibits some deviation from the inverse of particle radius. Therefore, in current study, the thermodynamic model is in conjunction with MD to understand seeded crystallization in nano-confinement. The situations in b (complete wetting) and c (partial wetting) form the focus of current study. Crystallization temperatures as a function of seed particle size, seed particle orientation, and nano-confinement system size will be examined.

II. SIMULATION METHODOLOGY

A classical MD method was used to study the crystallization process. The glue potential was used to model atomic interaction between Au atoms.²⁷ A nanodroplet is cooled below melting temperature then crystallizes with a nanocrystal seed. This process mimics the experimental process wherein a liquid droplet generated by laser-induced melting recrystallizes seeded by unmelted nanocrystals. Both the seed particle and the droplet were kept at the same temperature, below the bulk melting point T_0 and subjected to NVT (canonical ensemble—moles N , volume V , and temperature T are conserved) to simulate the crystallization. In NVT simulation, Berendsen thermostat was used to maintain constant temperature (weak coupling to a thermal path with $\tau_T = 0.28$ ps). Note in NVT simulation, latent heat is

assumed to transport away to the surrounding instantaneously. The coupling parameter $\tau_T = 0.28$ ps was chosen based on several trial tests (data not shown) showing its capability to effectively evacuate latent heat without suppressing thermal fluctuations substantially.

Solid seeds were carved out of perfect face center cubic (FCC) crystals. They were heated to desired temperatures with heating rate of $\sim 3.5 \times 10^{10}$ K/s. Undercooled nano-droplets were prepared by first heating the nanocrystal above T_0 , then cooled from melt to designated temperatures with cooling rate of $\sim 3.5 \times 10^{10}$ K/s. The heating and cooling were realized by adding/subtracting non-translational kinetic energy to the atoms such that their aggregate momentum is conserved. The time step is 2.8 fs.

In each of the crystallization simulations, the solid seed and the nano-droplet were brought close to within 5 Å with same temperatures in the initial configuration ($t = 0$ s). In the initial configuration of the simulation system, the solid seed was positioned such that its crystallographic [100] direction was taken to be parallel to the X direction. Figure 2 illustrates two configurations defining different relative positions of the solid seed with respect to the nano-droplet. In the first configuration (denoted as [100] system), the inter-particle direction is set to be parallel to the [100] direction (Fig. 2(b)). For the second configuration (denoted as [111] system), the inter-particle direction is parallel to the [111] direction (Fig. 2(a)). MD visualization is realized by VMD (Visual Molecular Dynamics).

In order to identify crystallization, we used the method of bond order parameters.²⁸ The local structure around the particle i is given by,

$$\overline{q}_{lm}(i) = \frac{1}{N_b(i)} \sum_{j=1}^{N_b(i)} Y_{lm}(\hat{r}_{ij}), \quad (3)$$

where the sum runs over all $N_b(i)$ bonds that particle i has with its neighbors. The $\overline{q}_{lm}(i)$ are local order parameters. From the $\overline{q}_{lm}(i)$, we can construct local invariants

$$q_l(i) = \left[\frac{4\pi}{2l+1} \sum_{m=-l}^l |\overline{q}_{lm}(i)|^2 \right]^{1/2} \quad (4)$$

and

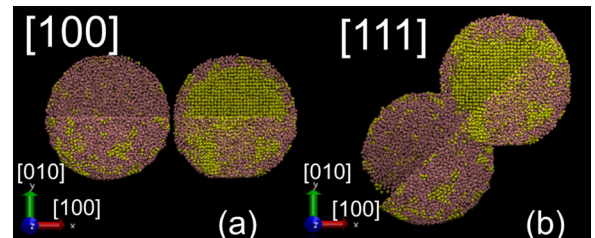


FIG. 2. A liquid nano-droplet is positioned in proximity to a nanocrystal seed to initiate crystallization. (a) In the first configuration (denoted as [100] system), the inter-particle direction is set to be parallel to the [100] direction. (b) For the second configuration (denoted as [111] system), the inter-particle direction is parallel to the [111] direction.

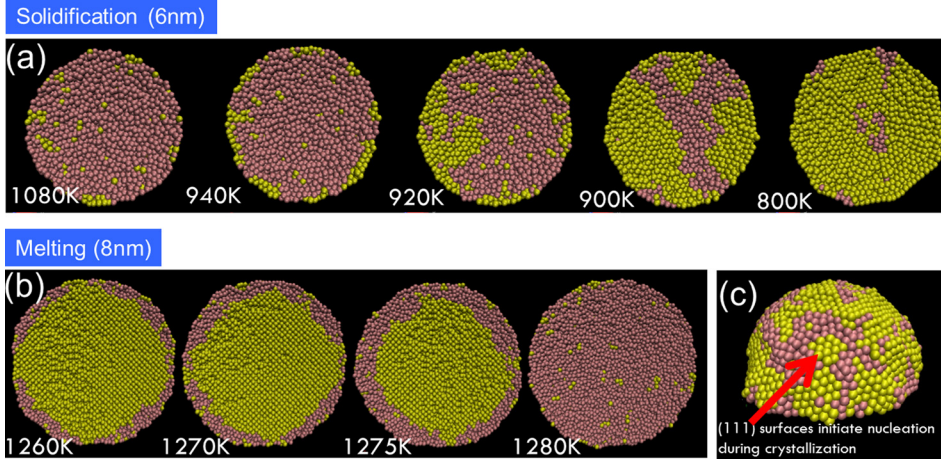


FIG. 3. Snapshots of MD simulation during solidification and melting of a single nanoparticle. Yellow colored atoms represent solid atoms identified by BOP and red colored atoms represent liquid/amorphous atoms. (a) Solidification process of a $D=6$ nm nanoparticle with cooling rate 1.74×10^{11} K/s; (b) melting process of a $D=8$ nm nanoparticle; (c) arrow indicates [111] surfaces that initiate nucleation during crystallization.

$$\hat{w}_l(i) = \frac{w_l(i)}{\left[\sum_{m=-l}^l |\bar{q}_m(i)|^2 \right]^{3/2}}. \quad (5)$$

These local order parameters are measures for the local order around particle i . $q_l(i)$ and $\hat{w}_l(i)$ ($q_4(i) < 0.13$ and $\hat{w}_4(i) > 0.07$) were used to distinguish hexagonal closed packed (HCP) atoms from other atoms.²⁹ We defined a dot product of the vectors q_6 of neighboring particle of i and j ,

$$q_6(i) \cdot q_6(j) = \sum_{m=-6}^6 \tilde{q}_{6m}(i) \tilde{q}_{6m}(j)^*, \quad (6)$$

and consider particle i and j to be "connected" if the dot-product exceeds 0.68. A particle is identified as solid-like if the number of connections with its neighboring particles exceeds 50% of all its neighbors.²⁴

III. SINGLE PARTICLE MELTING AND SOLIDIFICATION

We started with single nanoparticle melting and solidification in order to calibrate our methodology in studying phase transitions. Figure 3(a) shows snapshots of the cross section of a gold liquid droplet ($D=6$ nm) during cooling. With the cooling rate $\sim 1.74 \times 10^{11}$ K/s, nuclei initially appear at the droplet interior surfaces at ~ 940 K. As temperature decreases, the solid-liquid interface propagates toward the center. Under the current cooling rate, multiple nuclei can initiate from different sites on surface and successfully grow above critical nuclei size leading to multi-crystal morphology when fully crystallized. Closer examination at the surface (Fig. 3(c)) reveals that the nucleation initiates from (111) surfaces sites in agreement with the observations.^{23,30} It is known that the surface nucleation requires $\gamma_{sv} < \gamma_{ls} + \gamma_{lv}$ thermodynamically. The fact that nucleation initiates from (111) solid surfaces (low energy surfaces) could satisfy this thermodynamic requirement.

The bulk melting point of gold T_0 predicted by glue potential is 1357 K (Ref. 27) and experimental value is 1336 K.²⁷ Figure 3(b) illustrates the cross sections during the melting of a nanoparticle ($D=8$ nm). Figure 3(b) shows clear surface melting, during which the solid core and liquid

shell coexist, from 1260 K to 1275 K. Subsequently at 1280 K, the solid core of the nanoparticle uniformly melts inward. Before the particle is heated to its melting point T_{m1} (heating from 300 K), the particle exhibits truncated octahedral structure³¹ as shown in Figure 4 ($D=6$ nm, $T=1100$ K). The truncated octahedral structure is covered by (100) and (111) facets with the (100) facets partially covered by surface melting layer to minimize surface energy. The truncated octahedral structure of the single crystal seed particle is a result of balance between total surface energy and total elastic strain energy.³¹⁻³³

In order to obtain melting temperatures, a single nanoparticle was heated to desired temperatures with ΔT increments. At each temperature, the system was allowed to relax for 3×10^5 steps. During this interval, the potential is monitored to decide whether melting is occurring. ΔT is chosen based on computational cost. If the solid particle melts into liquid at $T+0.5\Delta T$ and remains solid at $T-0.5\Delta T$, we claim the melting temperature T_{m1} to be $T \pm 0.5\Delta T$. Such obtained melting points are 1049.7 ± 1.5 K ($D=4$ nm), 1140.2 ± 1.5 K ($D=5$ nm), 1184.2 ± 1.0 K ($D=6$ nm), 1227.5 ± 2.5 K ($D=8$ nm), 1252.5 ± 2.5 K ($D=10$ nm), and 1277.5 ± 2.5 K ($D=12$ nm). Note that larger ΔT is chosen for larger particles mainly due to computational cost consideration. Melting points are then plotted in Figure 5(a). The melting points can be fitted with the Pawlow equation after ignoring the density difference between liquid and solid phases (By MD simulation, the volume of an undercooled

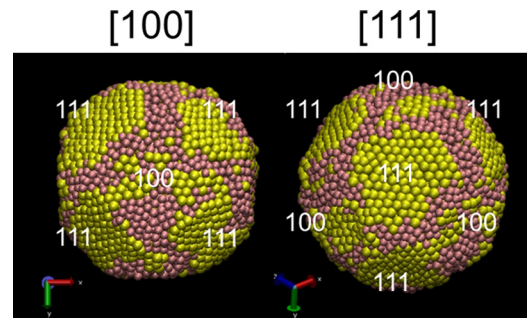


FIG. 4. The truncated octahedral nanocrystal ($D=6$ nm) is formed by heating a spherical solid particle to below melting temperature. The figure shows the atomic configuration viewed from [100] and [111] directions.

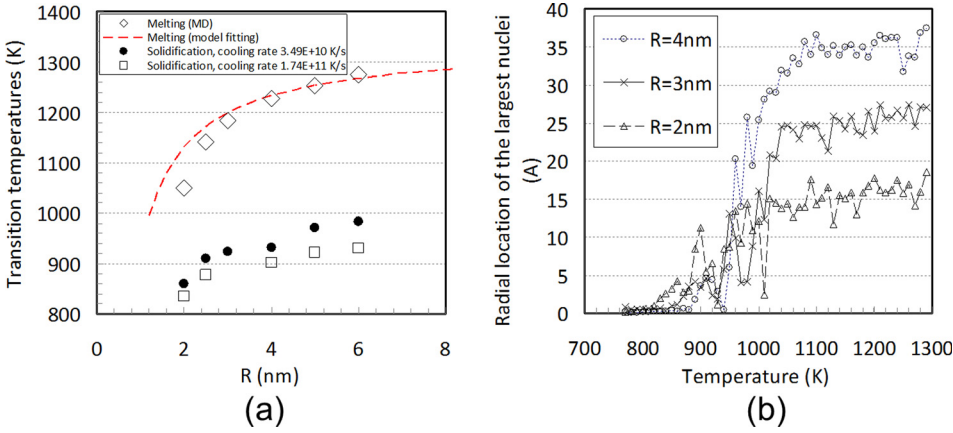


FIG. 5. (a) Melting points and crystallization points calculated from MD simulation for various nanoparticle sizes. The melting points are fitted by Pawlow equation shown as the red dashed curve. (b) Radial location of the largest nuclei during crystallization (cooling) in the droplet. The cooling rate is 1.74×10^{11} K/s.

droplet was compared with the volume of the same droplet after crystallization at the same temperature to estimate the density difference. The difference is estimated to be 1%–2%) as follows:

$$T_{m1} - T_0 = -\frac{2T_0v}{R_S\Delta H}(\gamma_{sv} - \gamma_{lv}). \quad (7)$$

By using Eq. (7) and assumed parameters ($T_0 = 1357$ K, $\Delta H = 0.12$ eV, and $v = 0.017$ nm³), the fitting parameter $\gamma_{sv} - \gamma_{lv}$ is found to be 0.18 J/m² in reasonable agreement with recorded data in literature (For experimental measurement of gold, $\gamma_{lv} = 1.13$ J/m², $\gamma_{sv} = 1.40$ J/m², and $\gamma_{ls} = 0.27$ J/m²;³⁴ for Embedded Atom Method potential,

$\gamma_{lv} = 0.74$ J/m², $\gamma_{sv} = 0.90$ J/m², and $\gamma_{ls} = 0.11$ – 0.16 J/m²). Solidification transition points are also obtained with two cooling rates. The melting and solidification temperatures can differ from 200 K to 400 K. In general, superheating is less likely to be observed during the melting, while undercooling is observed during solidification as a dominant process parameter. To quantify the nucleation initiation, Figure 5(b) plots the radial location of the largest nucleus that has the impetus to grow the fastest. Such a nucleus typically forms at the nanoparticle surface, independent of the particle size. As temperature decreases and the solidification transition proceeds, the center of the largest nucleus quickly moves towards the center.

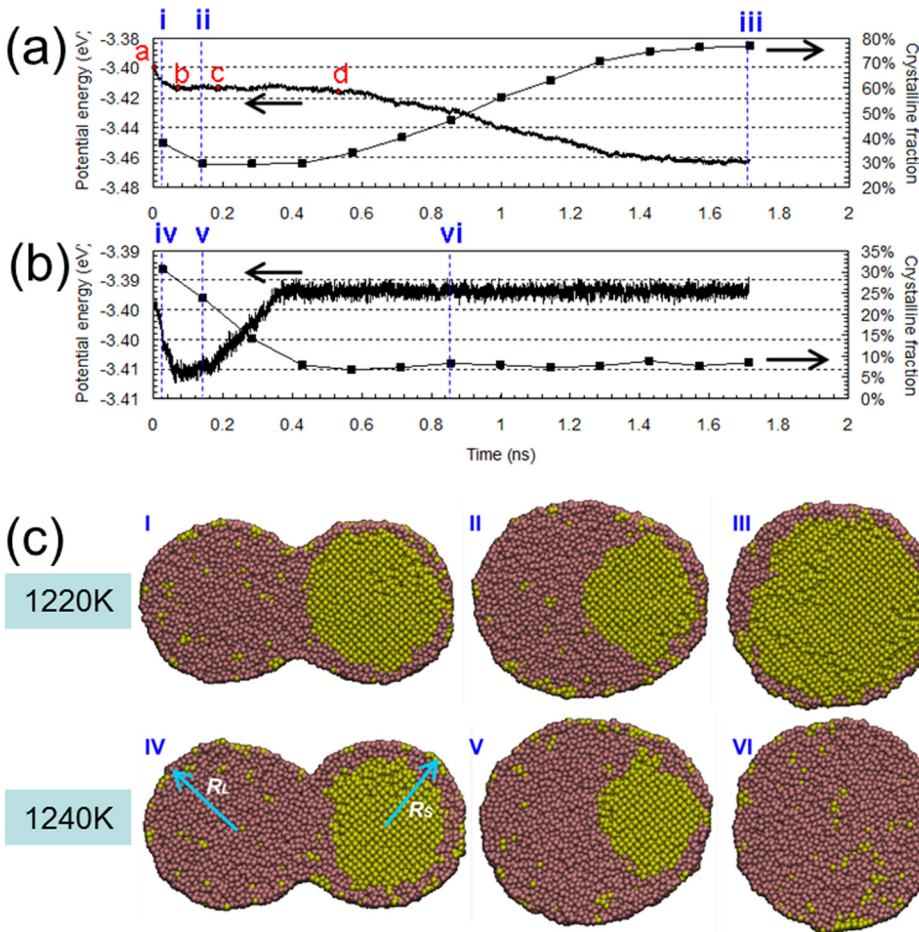


FIG. 6. Plots of potential energy (solid line) and crystalline fraction (line with symbols) evolutions during the nanocrystallization process for two temperatures: (a) 1220 K—crystal grows, events (a)-(d) are discussed in the main text; (b) 1240 K—crystal melts. The liquid and solid particles are 8 nm in diameter. (c) Snapshots of cross sections at different times indicated by i-vi. Yellow colored atoms represent solid atoms and red colored atoms represent liquid/amorphous atoms. R_L (R_S) is radius of liquid (solid) particle.

IV. CRYSTALLIZATION OF A NANO-DROPLET SEED BY A NANOCRYSTAL

We have explored so far the melting and solidification of isolated nanoparticles. We will focus this section on the crystallization of a liquid droplet seeded by a solid seed using NVT as described in Sec. II. In order to investigate the crystallization process, the time evolutions of the potential energy and crystal fraction calculated by bond order parameters (BOP) are shown in Fig. 6 along with snapshots of the crystal re-growth process. The potential energy plot in Fig. 6(a) shows that during the initial stage (a) \rightarrow (b), the system experiences a sharp reduction in potential energy. This is due to the reduction in surface energy when two particles initially contact. After the initial contact, from (b) \rightarrow (d), the system goes through a relatively flat transition in potential energy. The crystalline fraction calculated by BOP reveals between (i) and (ii) (<0.2 ns after contact), the solid seed undergoes partial melting, and the solid fraction reduces by $\sim 9\%$.

Thermodynamics suggest the liquid droplet tends to completely wet the solid particle, since the condition of partial wetting requires $\gamma_{sv} < \gamma_{ls} + \gamma_{lv}$. However, as described previously in Fig. 4, there exist low energy (111) surfaces on solid seed. Therefore, the wetting process may proceed until the solid seed is partially covered by the liquid droplet and partially covered by (111) surfaces as illustrated by Figures 6c-ii and 6c-v.

The plateau in potential energy between c and d in Figure 6(a) represents the liquid-solid coexistence. If the

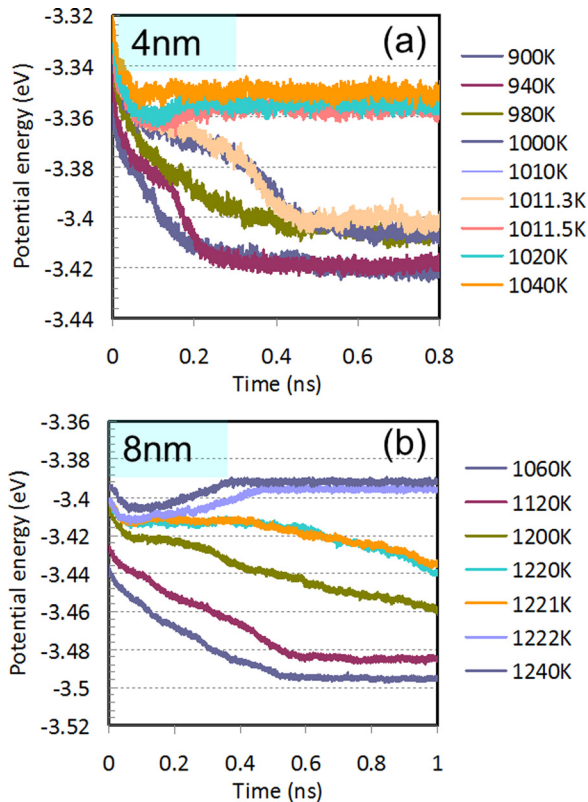


FIG. 7. Potential energy evolutions at different temperatures with fine temperature increments in order to identify transition temperature T_{m2} . (a) 4 nm solid particle with 4 nm liquid particle; (b) 8 nm solid particle with 8 nm liquid particle.

plateau can be maintained, it indicates the system has reached liquid-solid equilibrium. However, for the two temperatures 1220 K and 1240 K illustrated in Figure 6, neither could reach equilibrium. At 1220 K, the crystallization starts at around 0.4 ns as indicated by a gradual increase in crystalline fraction and decrease in potential energy until the $\sim 80\%$ of the system turns into solid. At a slightly higher temperature at 1240 K, the initial transition from (a) \rightarrow (b) can still be seen. However, the solid seed quickly dissolves into liquid indicated by an increase in potential energy accompanying monotonically decreasing crystalline fraction.

A. Crystallization temperatures

In order to obtain the crystallization temperatures T_{m2} of a liquid droplet seeded by a solid crystal, we prepared a series of samples pairing a solid seed and a liquid droplet with various sizes at various temperatures. Each sample is kept at different undercooling temperatures isothermally for a period of time as shown in Figure 7. The largest equilibrium time (plateau between b and d in potential energy plot) is about 0.4–0.5 ns for the system of two 8 nm particles with temperature increment, $\Delta T = 1$ K. For the system of two 4 nm particles, no observable plateau can be found even though the temperature increment $\Delta T = 0.5$ K. The reason for the longer equilibrium time for the large system is related to thermal fluctuations: the larger the system size, the smaller the fluctuations, thus the longer lag time.³⁵ Besides thermal fluctuation, our system also involves a dynamic surface wetting process upon initial contact of the two particles. Therefore, none of the systems could reach equilibrium within the scope of current study. Due to this reason, we could only locate T_{m2} in a range bounded by artificially selected ΔT . If the solid seed dissolves into liquid at $T + 0.5\Delta T$ and starts to grow if $T - 0.5\Delta T$, we claim the transition temperature T_{m2} to be $T \pm 0.5\Delta T$. Table I and Figure 8(a) summarize the crystallization temperatures T_{m2} for [100] and [111] systems along with the melting points obtained previously for single solid particle T_{m1} .

As expected, all transition temperatures are below the bulk melting temperature of 1357 K due to confinement effects. In the case of crystallization seeded by a solid particle, the transition temperature T_{m2} correlates strongly with seed particle sizes. To understand the dependence of T_{m2} on R_S , we invoke a two-sphere model. Consider a non-melting

TABLE I. Crystallization temperatures of liquid droplets seeded by solid particles and melting temperatures of solid particles.

R_S (nm)	R_L (nm)	Crystallization temperature T_{m2} (K)		Melting temperature T_{m1} (K)	
		T_{m2} [100]	T_{m2} [111]	R_S (nm)	T_{m1}
2.00	2.00	1011.4 \pm 0.1		2.0	1049.7 \pm 1.5
2.00	4.00	990.0 \pm 10.0			
3.00	3.00	1159.5 \pm 0.5	1170.0 \pm 10.0	3.0	1184.2 \pm 1.0
3.00	6.00	1110.0 \pm 10.0	1150.0 \pm 10.0		
4.00	4.00	1221.0 \pm 1.0	>1225.0	4.0	1227.5 \pm 2.5
5.00	5.00	1250.0 \pm 10.0		5.0	1252.5 \pm 2.5
6.00	6.00	1270.0 \pm 10.0		6.0	1277.5 \pm 2.5

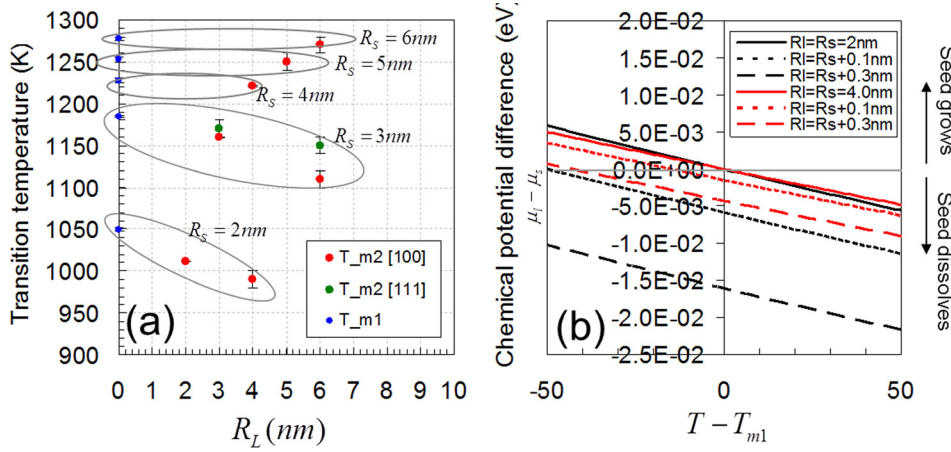


FIG. 8. (a) Crystallization temperatures with various seed particle sizes R_S and liquid droplet sizes R_L . T_{m1} is crystallization temperature of a single solid particle. T_{m2} [100] is crystallization temperature of two particles (a solid and a liquid) with inter-particle direction parallel to the [100] direction. T_{m2} [111] is crystallization temperature of two particles (a solid and a liquid) with inter-particle direction parallel to the [111] direction. (b) Chemical potential difference between a liquid particle and a solid particle. Negative value of $\mu_l - \mu_s$ (lower chemical potential in liquid phase) leads to seed melting.

(NM) case (where seed particle is completely covered with {111} facets, therefore, lower part of the seed particle is not wetted, Figure 9(a)) and surface melting (SM) case (where entire seed particle is covered by liquid, Figure 9(b)). Since the gold nanoparticle considered in this study has (111) and (100) facets, its characteristics should fall between the NM and SM cases. Following classical two-sphere model and heterogeneous nucleation theory³⁶ for the NM case, Gibbs free energy difference induced by moving the liquid-solid interface by δR_S (the gray area), $\delta G/\delta R_S$, is equal to zero when $R_S = r^* = 2\gamma_{ls}v/\Delta\mu$, where r^* is critical nuclei radius and $\Delta\mu$ is the driving force for crystallization $\Delta H(T_0 - T)/T_0$. Therefore, the crystallization/transition temperature for a solid seed of size R_S partially wetted by a droplet of R_L can be written as $T_{m2} = T_0 - \frac{2T_0\gamma_{sv}}{R_S\Delta H}$, which is not a function of the liquid droplet size R_L . For SM model, it is easy to show that, if the solid-to-liquid density variation is negligible: $v_s - v_l \sim 0$, the dependence of T_{m2} can be written as $T_{m2} = T_0 - \frac{2T_0\gamma_{sl}v}{R_S\Delta H}$. Therefore, both SM and NM models lead to same transition temperature T_{m2} and it is inversely proportional to R_S .

The above discussion explains the primary dependence of T_{m2} on R_S ; however, Figure 8(a) also shows that T_{m2} as obtained from droplet-seed system are lower than the melting points T_{m1} . In addition, the offset between T_{m1} and T_{m2} increases with liquid droplet diameter R_L and decreases with

solid seed diameter R_S for the all droplet-seed systems considered. As discussed previously from the two-sphere model, under equilibrium condition T_{m2} is not a function of the liquid droplet size R_L . We argue the observed dependence of T_{m2} on R_L is caused by the non-equilibrated and transient chemical potential imbalance between liquid and solid particles upon initial contact, as discussed in the following.

To understand the offset between T_{m1} and T_{m2} , we recall the Pawlow equation (Eq. (7)). This equation shows that at T_{m1} , the chemical potentials are equal between a solid and liquid particle with the same size R_S . Assuming departures of dT and dp away from equilibrium, the induced chemical potential variations ($d\mu$) between the two phases can be written as,

$$d\mu_l - d\mu_s = v_l dp_l - v_s dp_s - \frac{\Delta H}{T} dT. \quad (8)$$

Integrating from T_{m1} to T and R from R_S to R_L , we obtain at any temperature T (invoking $dp = d\left(\frac{2\gamma}{r}\right)$, and $v_s = v_l$)

$$\begin{aligned} \mu_l - \mu_s &= v_l \int_{R_S}^{R_L} d\left(\frac{2\gamma_{lv}}{r}\right) - \int_{T_{m1}}^T \frac{\Delta H}{T} dT \\ &= 2\gamma_{lv}v_l \left(\frac{1}{R_L} - \frac{1}{R_S}\right) - \Delta H \ln\left(\frac{T}{T_{m1}}\right). \end{aligned} \quad (9)$$

Expanding the logarithmic term by a Taylor series accurate to the 1st order

$$\mu_l - \mu_s = 2\gamma_{lv}v_l \left(\frac{1}{R_L} - \frac{1}{R_S}\right) + \Delta H \left(1 - \frac{T}{T_{m1}}\right). \quad (10)$$

This equation reveals the chemical potential difference between a pair of an isolated liquid droplet of radius R_L and a solid seed of radius R_S at various temperatures T in relation with the melting point T_{m1} of the solid particle. The value of $\mu_l - \mu_s$ will dictate how system evolves—negative value leads to melting of solid seed and vice versa.

Examining Eq. (10) reveals that larger R_L and smaller R_S will lead to solid seed melting, in which case T needs to be substantially lower than T_{m1} to drive the system towards crystallization. This helps explaining the observed R_L and R_S dependence in Fig. 8(a). To better illustrate this point,

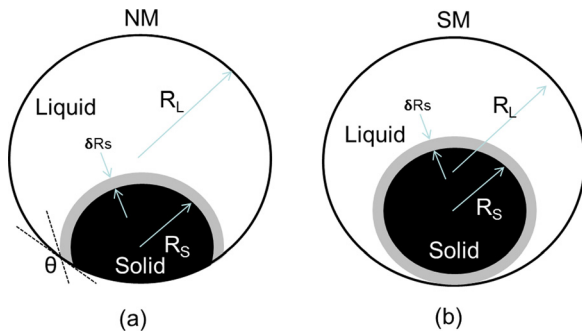


FIG. 9. Two-sphere model for case (a) where the solid seed is partially wetted—it is called non-melting (NM) case, (b) where the solid seed is completely wetted—it is called surface-melt (SM). R_L (R_S) is radius of liquid (solid) particle. δR_S is the incremental increase of solid particle radius as a result of crystallization. θ is the contact angle: $\gamma_{sv} = \gamma_{ls}\cos(180 - \theta) + \gamma_{lv}$.

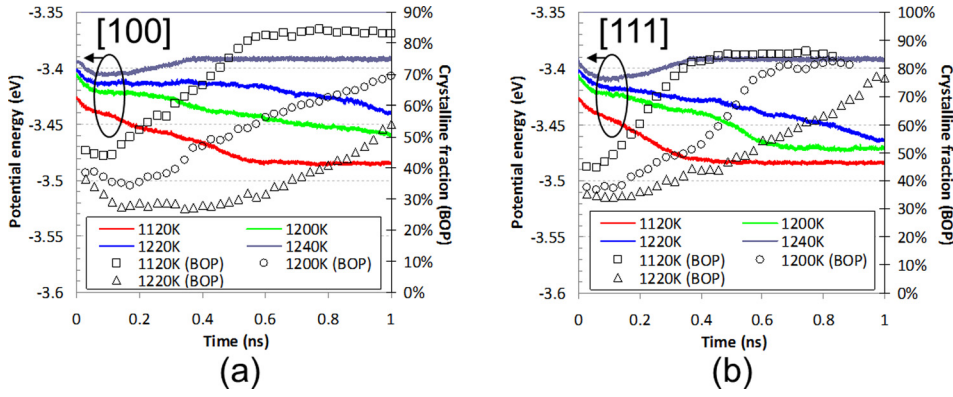


FIG. 10. Potential energy and crystalline fraction evolutions in (a) [100] direction and in (b) [111] direction. Solid lines represent potential energy and symbols represent crystalline fraction (BOP). It is seen that partial melting is less obvious in [111] direction as compared to [100] direction.

Figure 8(b) plots the chemical potential differences for two cases: one case $R_S = 2$ nm (black lines) and the other case $R_S = 4$ nm (red lines) with various R_L slightly larger than R_S in each case. The following findings can be seen, which explain observations in Fig. 8(a) better.

First, the results suggest that for a certain solid size R_S , the larger the droplet size R_L , the lower the chemical potential in the liquid phase and, therefore, the stronger driving force towards dissolving the seed. This is the reason when two particles contact, there exists a tendency of the solid seed particle to melt initially. In order to move the system towards crystallization, a lower temperature T and larger undercooling (defined as $T_{m1} - T$) is required therefore leading to a lower T_{m2} . This can be clearly seen from the MD simulation results in Figure 8(a) and Table I: in the case of $R_S = 3.0$ nm, when $R_L = 3.0$ nm, $T_{m2} = 1159.5 \pm 0.5$ °C and when $R_L = 6.0$ nm, T_{m2} is reduced to 1110.0 ± 10.0 °C. Furthermore, the dependence of chemical potential difference on R_L appears to be stronger for smaller R_S . This can be seen in Fig. 8(b) where the tendency towards melting (negative $\mu_l - \mu_s$ value) is less for $R_S = 4$ nm (red lines) than that for $R_S = 2$ nm (black lines).

Second, the chemical potential difference between liquid and solid phases appears to be stronger for smaller R_S . In other words, larger R_S requires less undercooling to drive the system into the crystallization direction. The results can also be seen from MD simulation (Fig. 8(a)) in that the difference between T_{m1} and T_{m2} diminishes with increase of R_S .

Finally, Fig. 8(b) indicates when $R_S = R_L$, any temperature below T_{m1} should lead to crystallization. In MD simulation, with $R_S = R_L = 4$ nm in [111] orientation, at any temperature below T_{m1} , crystallization occurs (Table I). However, the same results cannot be seen for [100] direction, where T_{m2} is always found to be lower than T_{m1} , even when $R_S = R_L$. The discrepancy is due to the fact that after two particles contact, interface reconstruction will occur as a result of minimizing interfacial energy and elastic strain in solid particle locally. The transient development is sensitive to the seed particle orientation. The above simple analysis based on chemical potentials of two isolated particles is not adequate. Detailed analysis between [100] and [111] orientations will be covered in Sec. IV B.

One could argue that smaller system could be closer to equilibrium (needs less time to relax); therefore, the above described non-equilibrated model may not be equally valid for smaller system. It should be noted that the dependence

of chemical potential imbalance on $-1/R_S$ (Eq. (10)) suggests smaller system is actually in a more non-balanced condition to start with and will require longer time to be relaxed. Furthermore, before reaching equilibrium, the system will experience partial melting (reduction in R_S), which will have higher impact on smaller system. Therefore, we conclude non-equilibrium condition will have similar effect on smaller system (if not more) as larger system although smaller system is considered to be closer to equilibrium in general.

B. Difference between [100] and [111] orientations

In order to understand the difference between the [100] and [111] orientations, Figure 10 compares the potential and crystalline fraction evolution of the [111] and [100] systems. The comparison shows that at the same temperature, the potential energy drops appear to be slower for [100] systems. Figure 10(a) shows that the initial reduction in crystalline fraction (<0.4 ns) in [100] system becomes more obvious with increasing temperature from 1120 K to 1220 K. In contrast, these drops are not obvious in the [111] system. The initial partial melting resulting in reduction in the solid particle size then requires lower crystallization temperatures.

Detailed probing of the atomic arrangement during the crystallization process can be seen in Figure 11 (view in [110] direction). The liquid and amorphous atoms have been

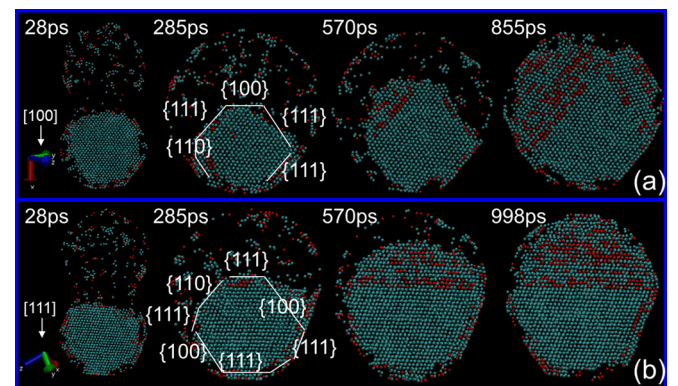


FIG. 11. Atomic configurations during initial interface reconstruction and subsequent crystal growth (view in [110] direction) for (a) [100] orientation and (b) [111] orientation. In [100] orientation (a), liquid-solid interface breaks into {100} and {111} interfaces. In [111] orientation (b), {111} interfaces are largely maintained.

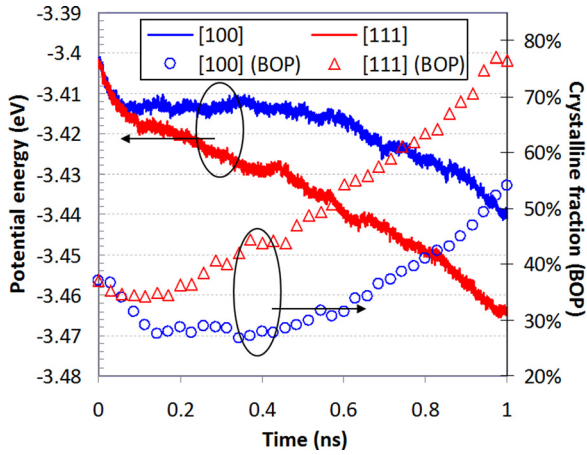


FIG. 12. Detailed potential energy and crystalline fraction evolutions during initial interface reconstruction and partial melting for [100] and [111] directions.

omitted for clearer representation. Once the liquid droplet contacts the solid particle surface at $t = 28$ ps, the droplet immediately wets the solid particle surfaces that are directly facing the droplet including the non-melted (111) facets. In the [100] direction, a tendency for the formation of additional facets established on (111) crystal planes can be clearly seen. This is accompanied by the reduction of solid particle size. A similar phenomenon has been observed on Si (100) surface upon melting.^{37,38} The structure of the interface is governed by the potential energy, stress, and entropic factors. Close-packed (111) liquid-solid interfaces have been reported to have the lowest energy using capillary fluctuation method,⁴⁰ cleaving method,^{41,42} and the recently introduced integration method.^{39,43–45} Therefore, the (100) interface has an unstable macroscopic orientation and will evolve toward

a stable state as a consequence of the spontaneous formation of facets with two (or more) different orientations. In the case of [100] direction, the interface breaks into (100) and (111) interfaces as a result of reduction of (100) interfaces and increase of (111) interfaces. On the other hand, in the case of the [111] orientation, the liquid-solid interfaces are much closer to the (111) surfaces and therefore the interface largely maintains its original (111) interfaces, avoiding exposure of (100) surfaces.

A closer examination of the potential energy plot for the [100] and [111] directions can provide enhanced understanding regarding the difference between the two orientations during the initial melting. In Figure 12, for both [111] and [100] orientations, rapid drops in potential energy are seen for $t < 0.2$ ns, due to reduction in surface energy. During the same period of time, both systems undergo melting with 2.7% (in [111]) and 9.5% (in [100]) atoms melted. The potential energy should increase by $2.7\% \times 0.12 \text{ eV} = 0.0032 \text{ eV}$ and $9.5\% \times 0.12 \text{ eV} = 0.0114 \text{ eV}$ in [111] and [100] systems, respectively, as a result of melting. Here, 0.12 eV is the latent heat per atom in liquid-solid transition. Interestingly, neither system shows any increase in potential energy during $t = 0$ to $t = 0.2$ ns, but on the contrary, decrease by 0.02 eV and 0.014 eV can be seen in [111] and [100] directions, respectively. This suggests that purely from the potential energy point of view, the reduction in potential energy (including surface energy reduction upon contact and the disappearing of high energy liquid-solid interfaces discussed above) during the interface reconstruction is sufficient to compensate the increase in potential energy induced by the initial melting. Fundamentally, the driving force of the initial melting and reconstruction to expose (111) planes is a result of minimization of Gibbs free energy that includes the entropic factors

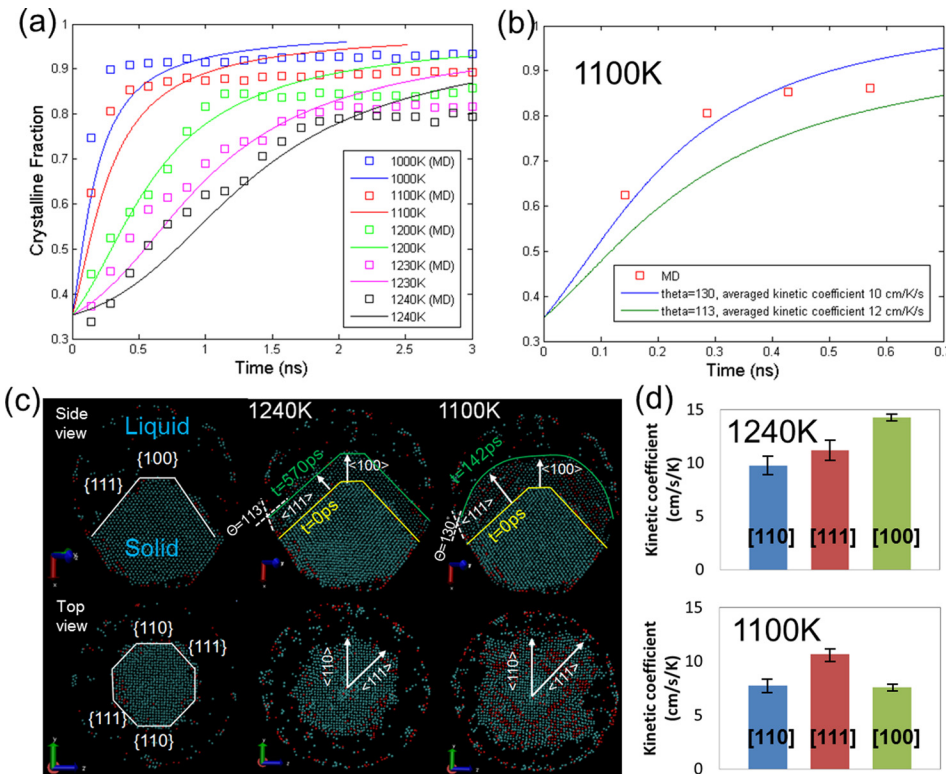


FIG. 13. (a) Calculated crystallization velocity $V = \mu(T_{m2} - T)$ and transient crystal growth rate in comparison with MD simulation ($R_s = R_L = 5$ nm). Solid lines are calculated values and symbols are MD simulation results. (b) Transient crystal growth predicted with different interfacial profiles. The contact angle θ is used to adjust the interface profile. A semi-spherical/curved interface (larger θ) effectively increases crystal growth rate. (c) Atomic details on interfacial profiles during crystallization for two temperatures (1240 K and 1100 K). Yellow profile outlines the interface before crystal growth, and green profile outlines the profile after crystal growth. The green outlines a semi-spherical/curved profile (larger θ) at 1100 K, while a flat profile is found at 1240 K. (d) Measured kinetic coefficients in [110], [111], and [100] directions. The curved interface at 1100 K is due to suppressed [100] growth.

and stress/strain components. In addition, the equilibrium shape of the solid crystal can depend on particle size. In a dynamic equilibrium situation, the (111) planes are also the slowest to melt. The detailed analysis of interface reconstruction is beyond the scope of this work and will be reported separately.

C. Crystallization velocity

To shed light into the dynamic crystal growth process in the nano-confinement, we perform crystallization velocity computation analytically and compared with MD simulations. Using transition temperature $T_{m2} = T_0 - \frac{2T_0\gamma_{sl}v}{R_s\Delta H}$ derived previously, interfacial velocity can be calculated by $V = \mu(T_{m2} - T)$, where μ is interfacial kinetic coefficient (averaged among (100), (111), and (110) facets). The computed velocity is coupled with the two-sphere model (NM) to obtain transient crystal fraction evolution during the crystallization: the velocity is used to increase R_s by $\delta R_s = V \delta t$ in the two-sphere model to predict crystal fraction as a function of time at constant temperature T . T_{m2} is updated with R_s in each iteration, and it is assumed $v = v_s = v_l$. The computed profiles are shown in Figure 13(a) for $R_s = R_L = 5$ nm using averaged kinetic coefficient $\mu = 12.0$ cm/K/s and $\theta = 113^\circ$ (following nomenclature from Cooper¹⁶). Better agreement between analytical model (lines in Fig. 13(a)) and MD results (symbols) can be found for temperatures ≥ 1200 K. At lower temperature, the model underestimates the crystallization progress. To understand detailed mechanism, we followed the solid-liquid interface movements at 1240 K and 1100 K and measured kinetic coefficients $\mu_{[100]}$, $\mu_{[110]}$, and $\mu_{[111]}$, respectively (Figs. 13(c) and 13(d)). First, it is found $\mu_{[100]}$ and $\mu_{[110]}$ are from ~ 10.0 to 15.0 cm/K/s (at 1240 K), which are slightly lower than reported values for glue potential ~ 12.6 – 18.8 cm/K/s,⁴⁶ while $\mu_{[111]}$ is found to be ~ 10 cm/K/s, which is higher than reported value ~ 7.0 cm/K/s.⁴⁶ It is well known that kinetic coefficient $\mu_{[111]}$ is lowest in un-confined system since part of driving force is dissipated in hesitating to select one of the phases.⁴⁶ However, in nano-confinement, $\mu_{[111]}$ is no longer the lowest: at 1240 K, $\mu_{[111]}$ is higher than $\mu_{[110]}$, and at 1100 K, $\mu_{[111]}$ becomes the highest. The nano-confinement effect reduces the coexistence of three phases and results in higher crystallization velocity for (111) facets.⁴⁶ Additionally, the tendency to avoid exposure of (100) and (110) facets suppresses the growth in those interfaces, especially at high undercooling (1100 K). As a result, the cone-shaped crystallization front (due to retarded growth at (111)) observed in 1240 K evolves into the semi-spherical front at 1100 K. To verify the impact of interfacial profile on crystallization, we performed the analytical modeling at 1100 K with $\theta = 130^\circ$ (to induce and mimic the curved interface) and $\mu = 10.0$ cm/K/s and compare with $\theta = 113^\circ$ and $\mu = 12.0$ cm/K/s. The higher θ value better reproduces the transient crystal growth verifying the curved interface accounts for faster crystallization process at high undercooling. It should be pointed out that the flat interface at low undercooling (1240 K) is now replaced with a curved interface at high undercooling, which could potentially lead to high defects.

V. SUMMARY AND CONCLUSIONS

To summarize, we have investigated the crystallization of a melt nanodroplet seeded by a nanocrystal using molecular dynamics simulations. In NVT system, the nanodroplet and nanocrystal are both maintained below the bulk melting temperature. Contact, coalescence of the two particles, and subsequent droplet crystallization are studied in detail. The main conclusions can be summarized as follows:

- (1) Immediately after the contact of the liquid droplet with the seed particle, reconstruction of the liquid-solid interface occurs. Partial melting of the truncated octahedral solid particle can be observed. The amount of partial melting is higher in the [100] direction than that in the [111] direction.
- (2) The crystallization temperature, defined as the temperature below which a liquid droplet can completely crystallize, is mostly determined by the melting temperature of the solid seed particle, as can be explained by a two-sphere model. The size of the liquid droplet has secondary impact on the crystallization temperature. The larger the droplet size, the lower the crystallization temperature. Larger droplet size will have reduced chemical potential in the liquid phase, therefore, requiring higher undercooling to move the system into crystallization.
- (3) Crystallization temperature is lower in [100] direction than in the [111] direction, which is caused by higher degree of melting in [100] direction upon initial contact.

ACKNOWLEDGMENTS

Support to this work by the King Abdullah University of Science and Technology (KAUST) is acknowledged.

- ¹J. S. Im and H. J. Kim, *Appl. Phys. Lett.* **64**, 2303 (1994).
- ²S. D. Brotherton, *Semicond. Sci. Technol.* **10**, 721 (1995).
- ³G. Andrae, J. Bergmann, F. Falk, and E. Ose, *Thin Solid Films* **337**, 98 (1999).
- ⁴Y. Liu, M. D. Deal, and J. D. Plummer, *Appl. Phys. Lett.* **84**, 2563 (2004).
- ⁵M. Miyao, K. Toko, T. Tanaka, and T. Sadoh, *Appl. Phys. Lett.* **95**, 022115 (2009).
- ⁶K. Toko, T. Sakane, T. Tanaka, T. Sadoh, and M. Miyao, *Appl. Phys. Lett.* **95**, 112107 (2009).
- ⁷V. D. Cammilleri, V. Yam, F. Fossard, C. Renard, D. Bouchier, P. F. Fazzini, and M. Hytch, *J. Appl. Phys.* **106**, 093512 (2009).
- ⁸R. Matsumura, Y. Tojo, M. Kurosawa, T. Sadoh, I. Mizushima, and M. Miyao, *Appl. Phys. Lett.* **101**, 241904 (2012).
- ⁹Y. S. Woo, K. Kang, M. Jo, J. Jeon, and M. Kim, *Appl. Phys. Lett.* **91**, 223107 (2007).
- ¹⁰H. Arora, P. Du, K. W. Tan, J. K. Hyun, J. Grazul, H. L. Xin, D. A. Muller, M. O. Thompson, and U. Wiesner, *Science* **330**(6001), 214 (2010).
- ¹¹A. Chimmalgi, D. J. Hwang, and C. P. Grigoropoulos, *Nano Lett.* **5**, 1924 (2005).
- ¹²B. Xiang, D. J. Hwang, J. B. In, S. Ryu, J. Yoo, O. Dubon, A. M. Minor, and C. P. Grigoropoulos, *Nano Lett.* **12**(5), 2524–2529 (2012).
- ¹³O. Van Overschelde, G. Guisbiers, and M. Wautelet, *J. Phys. Chem. C* **113**(34), 15343–15345 (2009).
- ¹⁴H. Pan, N. Misra, S. Ko, C. P. Grigoropoulos, N. Miller, E. E. Haller, and O. Dubon, *Appl. Phys. A: Mater. Sci. Process.* **94**(1), 111 (2009).
- ¹⁵H. Pan, S. H. Ko, N. Misra, and C. P. Grigoropoulos, *Appl. Phys. Lett.* **94**(7), 071117 (2009).
- ¹⁶S. J. Cooper, C. E. Nicholson, and J. Liu, *J. Chem. Phys.* **129**, 124715 (2008).
- ¹⁷Ph. Buffat and J. P. Borel, *Phys. Rev. A* **13**(6), 2287 (1976).

- ¹⁸R. Kofman, P. Cheyssac, A. Aouaj, Y. Lereah, G. Deutscher, and T. Ben-David, *Surf. Sci.* **303**(1–2), 231 (1994).
- ¹⁹D. Schebarchov and S. C. Hendy, *Phys. Rev. Lett.* **96**, 256101 (2006).
- ²⁰P. Pawlow, *Z. Phys. Chem.* **65**(1), 545 (1909).
- ²¹H. Reiss and I. B. Wilson, *J. Colloid Sci.* **3**, 551 (1948).
- ²²C. R. M. Wronski, *Brit. J. Appl. Phys.* **18**, 1731 (1967).
- ²³H. S. Nam, N. M. Hwang, B. D. Yu, and J. K. Yoon, *Phys. Rev. Lett.* **89**(27), 275502 (2002).
- ²⁴E. Mendez-Villuendas and R. K. Bowles, *Phys. Rev. Lett.* **98**, 185503 (2007).
- ²⁵H. Pan, S. Ko, and C. P. Grigoropoulos, *J. Heat Transfer* **130**, 092404 (2008).
- ²⁶Y. Shibuta and T. Suzuki, *J. Chem. Phys.* **129**, 144102 (2008).
- ²⁷F. Ercolessi, M. Parrinello, and E. Tosatti, *Philos. Mag. A* **58**(1), 213–226 (1988).
- ²⁸P. J. Steinhardt, D. R. Nelson, and M. Ronchetti, *Phys. Rev. B* **28**, 784 (1983).
- ²⁹Y. Wang, S. Teitel, and C. Dellago, *Nano Lett.* **5**(11), 2174 (2005).
- ³⁰G. Opletal, C. A. Feigl, G. Grocholar, I. K. Snook, and S. P. Russo, *Chem. Phys. Lett.* **482**, 281–286 (2009).
- ³¹A. S. Barnard and P. Zapol, *J. Chem. Phys.* **121**(9), 4276 (2004).
- ³²S. J. Ino, *Phys. Soc. Jpn.* **27**, 941–953 (1969).
- ³³B. Wang, M. Liu, Y. Wang, and X. Chen, *J. Phys. Chem. C* **115**, 11374 (2011).
- ³⁴Y. G. Chushak and L. Bartell, *J. Phys. Chem. B* **105**, 11605 (2001).
- ³⁵X. Bai and M. Li, *J. Chem. Phys.* **122**, 224510 (2005).
- ³⁶N. H. Fletcher, *J. Chem. Phys.* **29**(3), 572 (1958).
- ³⁷U. Landman, W. D. Luedtke, R. N. Barnett, C. L. Cleveland, and M. W. Ribarsky, *Phys. Rev. Lett.* **56**(2), 155 (1986).
- ³⁸W. D. Luedtke, U. Landman, M. W. Ribarsky, R. N. Barnett, and C. L. Cleveland, *Phys. Rev. B* **37**(9), 4647 (1988).
- ³⁹B. B. Laird, R. L. Davidchack, Y. Yang, and M. Asta, *J. Chem. Phys.* **131**, 114110 (2009).
- ⁴⁰J. J. Hoyt, M. Asta, and A. Karma, *Phys. Rev. Lett.* **86**, 5530 (2001).
- ⁴¹J. Q. Broughton and G. H. Gilmer, *J. Chem. Phys.* **84**, 5759 (1986).
- ⁴²R. L. Davidchack and B. B. Laird, *Phys. Rev. Lett.* **85**, 4751 (2000).
- ⁴³T. Frolov and Y. Mishin, *J. Chem. Phys.* **131**, 054702 (2009).
- ⁴⁴T. Frolov and Y. Mishin, *Phys. Rev. B* **82**, 174114 (2010).
- ⁴⁵T. Frolov and Y. Mishin, *Phys. Rev. B* **82**, 174113 (2010).
- ⁴⁶F. Celestini and J. Debierre, *Phys. Rev. E* **65**, 041605 (2002).